

Anisotropic Uppermost Mantle in Young Subducted Slab underplating Central Mexico

Teh-Ru Alex Song¹ & YoungHee Kim²

Corresponding to Teh-Ru Alex Song (tehrusong@gmail.com)

1. Yokohama Institute for Earth Sciences, IFREE, JAMSTEC, 3173-25 Showa-machi, Kanazawa-ku, Yokohama City, Kanagawa, 237-0005, Japan.

2. Division of Geological and Planetary Science, California Institute of Technology, 1200. E. California Blvd. Pasadena, CA 91125. U.S.A

The nature of phase C

The amplitude of phase C is also about half that of the converted S-to-P waves (phase A and phase B, Fig. 2a) from the USL (Song et al. 2009). In addition, the phase C displays the same polarity as the phase B, which converts from the top of the USL with a positive velocity jump (velocity increases with depth across this interface). Because it is observed from events spanning different magnitude, complexities of earthquake sources are probably not relevant. Since phase C is not consistent with a down-going wave propagating through a high velocity gradient located beneath earthquake sources when tested against teleseismic receiver functions, we explore possibilities that phase C is also an up-going converted wave that interacts with an internal slab structure above the earthquake sources (see also Fig. 2a).

Lithology of the anisotropic layer

There are two candidates to explain the anisotropic layer (AL) in the subducting slab. First, it is possible that the AL represents a crustal component, such as eclogites (Hacker et al. 2003). However, for estimated subduction zone thermal structures, the observed location of the AL corresponds to a temperature range from 400°C to 500°C and pressure range from 0.8 to 1.6 GPa (Currie et al. 2004) (Fig. 1, Fig. 3), which represents too low a metamorphic grade for eclogite formation (Hacker et al. 2003). In addition, eclogitization presumably begins in more hydrated upper crust earlier than in less hydrated lowermost crust, due to kinetics. Furthermore, eclogite is weakly anisotropic and it is probably difficult to argue it as the origin of the AL. Alternatively, mantle rocks such as dunites display a stronger anisotropy (Ismail and Mainprice, 1998) than typical mantle harzburgites and are abundant in the uppermost mantle section of ophiolite outcrops (Christensen, 1979; 1984), a representation of a section of crust-mantle transition in the oceanic plate

Causes of the uppermost mantle anisotropy in the subducted slab

The orientation of the fast symmetry axis within the AML is consistent with the fabric foliation recorded in the mantle section of ophiolites (Nicolas and Violette, 1982; 1985; Ceuleneer et al. 1988). Along with laboratory experiments under anhydrous conditions appropriate for depleted ridge-environment uppermost mantle (Zhang and Karato, 1995) and predictions from simulations of seismic anisotropy near MORs (Blackman et al. 2002), the orientation of the fast symmetric axis in the AL shall help resolve anisotropy generation process that is either stress-driven or strain-driven and how it may be dictated by the competition between passive flow and active upwelling (Karato and Jung, 1998; Blackman et al. 2002). If the observed anisotropy in the AML is due to strain-induced lattice preferred orientation (LPO), the observed dipping direction of fast symmetric axis is not inconsistent with predictions by active upwelling. This conclusion strongly support that active upwelling due to melt-induced buoyancy is also involved in the East-Pacific Rise, as documented by regional and global surface wave tomography and anisotropy analysis (Forsyth et al. 1998).

Further comparisons of localized anisotropic layer in modern and fossil slabs

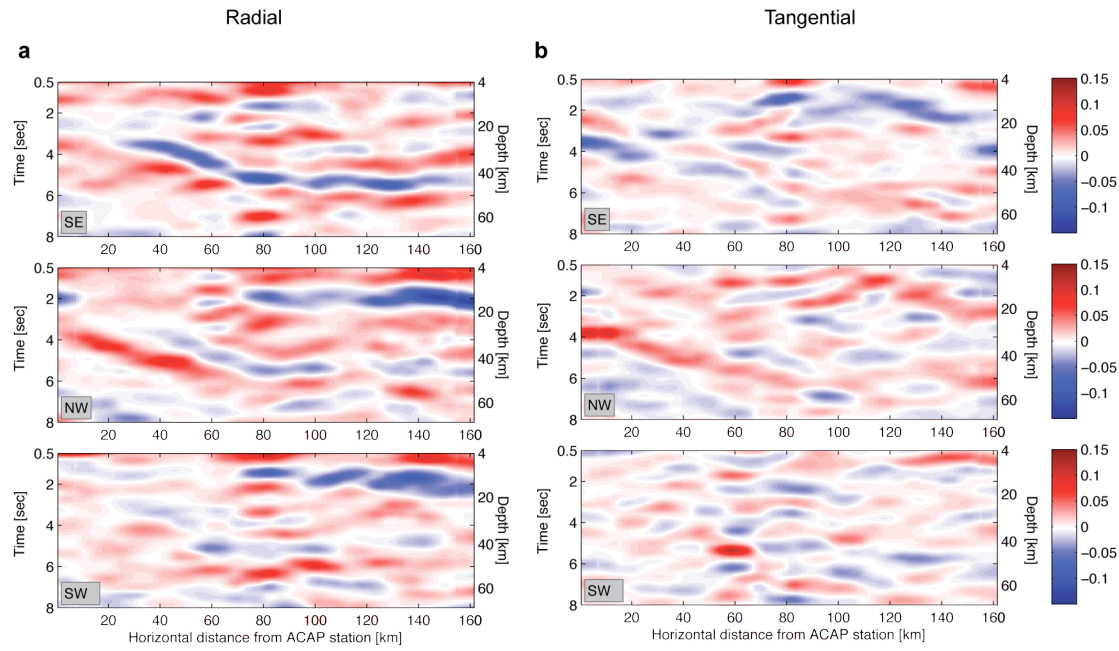
We refer dipping anisotropic layers beneath cratons (Bostock, 1997; Mercier et al. 2008; Masacchio et al. 2004; Bostock, 1999) as paleo-AMLS. There are some differences between the Cocos AML and paleo-AMLS beneath cratons. The AML within the Cocos plate is only 2-6 km thick, at least 2 times thinner than paleo-AMLS (~10 km). This difference in thickness can potentially be understood through recognition of thermal history of the Earth (Herzberg et al. 2010). As the mantle was probably hotter than the modern mantle by about 150-200°C (Herzberg et al. 2010; Sizova et al. 2010), it was likely to produce a larger degree of melting and to form ~25-35 km thick

oceanic crust, 3-5 times thicker than the modern oceanic crust. Likewise, the complementary oceanic mantle would have increased depletion, with a thicker layer of harzburgite lithology and likely much larger amounts of dunite formed by melt-mantle reaction near the paleo-Moho. The differences in thickness and magnitude of anisotropy in such a paleo-AML are a matter of speculation, but it is plausible that the anisotropic layer might have been significantly thicker. It is possible to preserve the paleo-AML during subduction if the deformation was limited above it and it is decoupled from the overriding sub-cratonic lithospheric mantle. The lack of compression in cratons over geological time suggests that the paleo-AML is likely decoupled from the overriding sub-cratonic lithospheric mantle, similar to processes associated with modern slab underplating beneath Central Mexico.

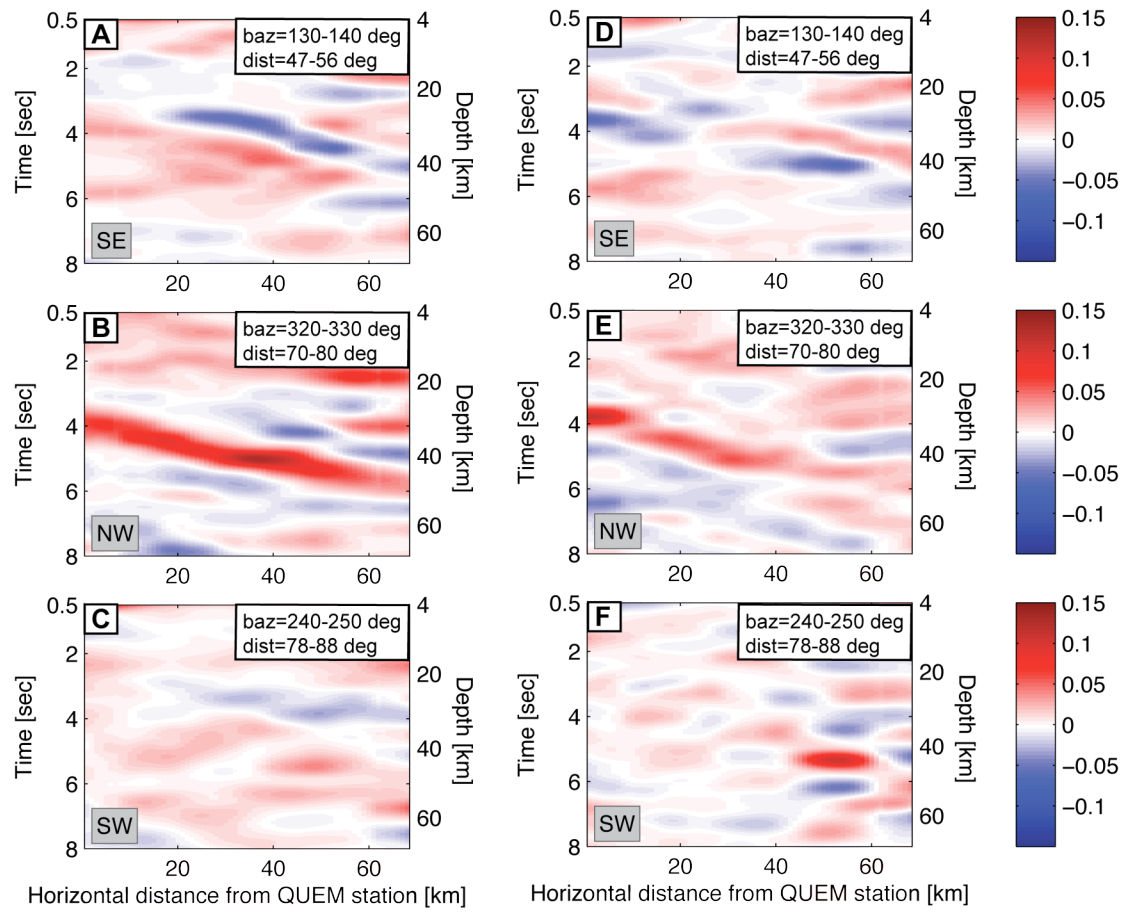
Inferences of paleo-spreading rates and implications on paleo plate kinematics

The half-spreading rate corresponding to the paleo-AML that subducted beneath the Wopmay Orogen at about 1.8 Ga (Mercier et al. 2008) is likely similar to or lower than that in the modern slow-spreading Mid-Atlantic ridge (~20 mm/yr) (Fig. 4). The half-spreading rate corresponding to the paleo-AMLS subducted at about 2.6 Ga beneath the western Slave craton (Bostock, 1997) and about 2.7 Ga beneath the Superior craton (Masacchio et al. 2004) are in the regime of fast spreading of about 50 mm/yr, similar to that of the northern East-Pacific Rise. The relatively steep fast symmetric axis in the paleo-AML could also indicate a stronger component of buoyancy-induce active upwelling in the parent mid-ocean ridge than that in the modern East-Pacific Rise. This inference may be recognized by consistency among the dip of fast symmetric axis of the AML, the paleo-AML and the orientation of foliations among different types of ophiolite outcrops that appear to be spreading-rate dependent (Nicolas and Violette, 1982; Boudier and Nicolas, 1985; Ceuleneer et al. 1988, see also Supplementary Fig. 15).

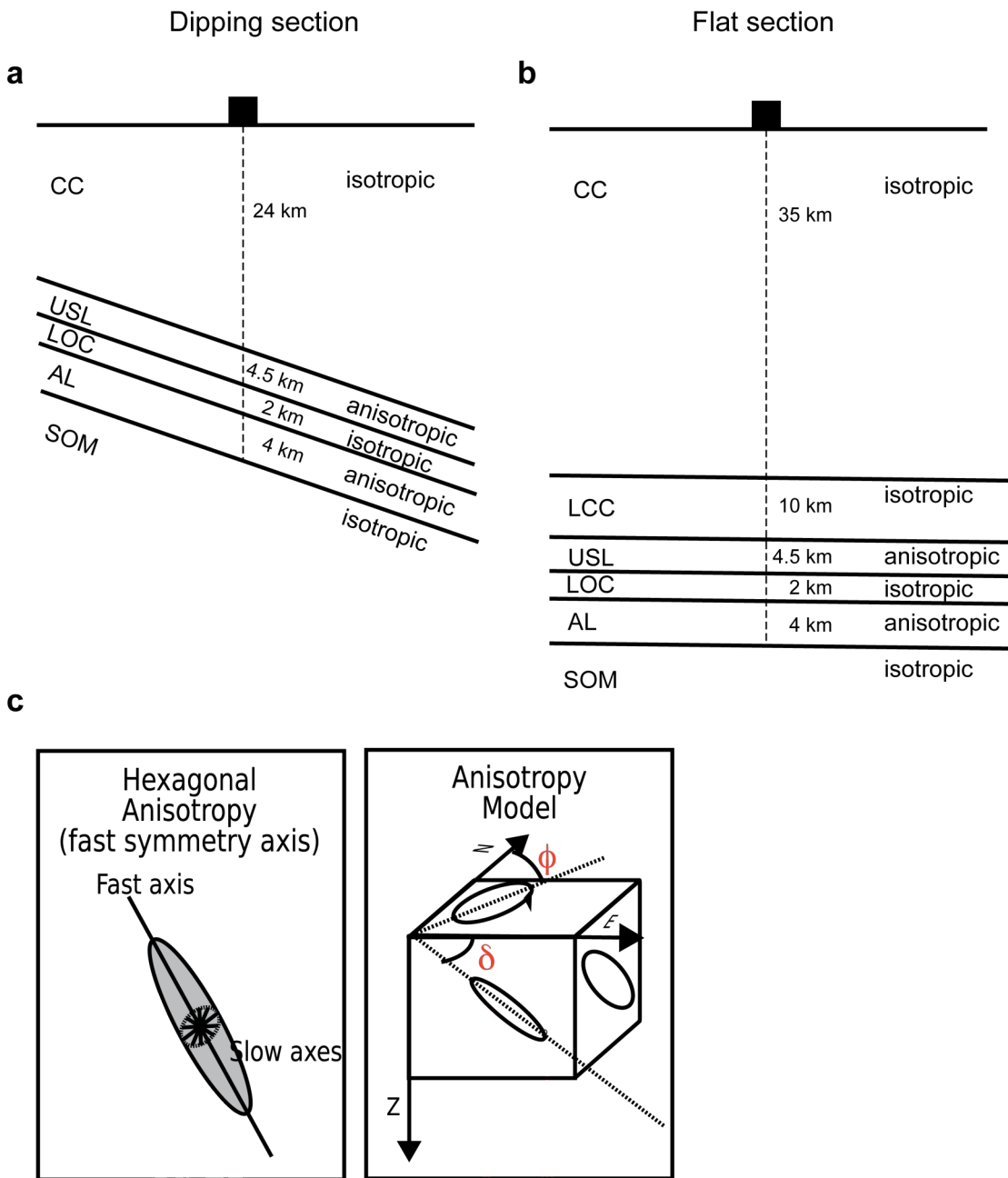
Together, these inferences provide a novel assessment of models related to plate kinematics and thermal evolution of the Earth (Korenaga, 2006). For example, tectonics of mid-ocean ridges and subduction have been inferred to play key roles in regulating the carbon cycle, sea water chemistry, climate and sea level changes over the long-term. We may tentatively speculate that decreases in spreading rates from 2.6-2.7 Ga to 1.8 Ga near North America cratons (Fig. 4) may be associated with episodic subductions (O'Neill et al. 2007) and a dispersal of a supercontinent (Silver and Behn, 2008). The inferred plate velocity during the assemblages and accretions of various tectonic terranes may be referenced against regional stratigraphic reconstruction (Hoffman and Bowring, 1984) and thermo-petrol-dynamical modeling (Faccenda et al. 2008).



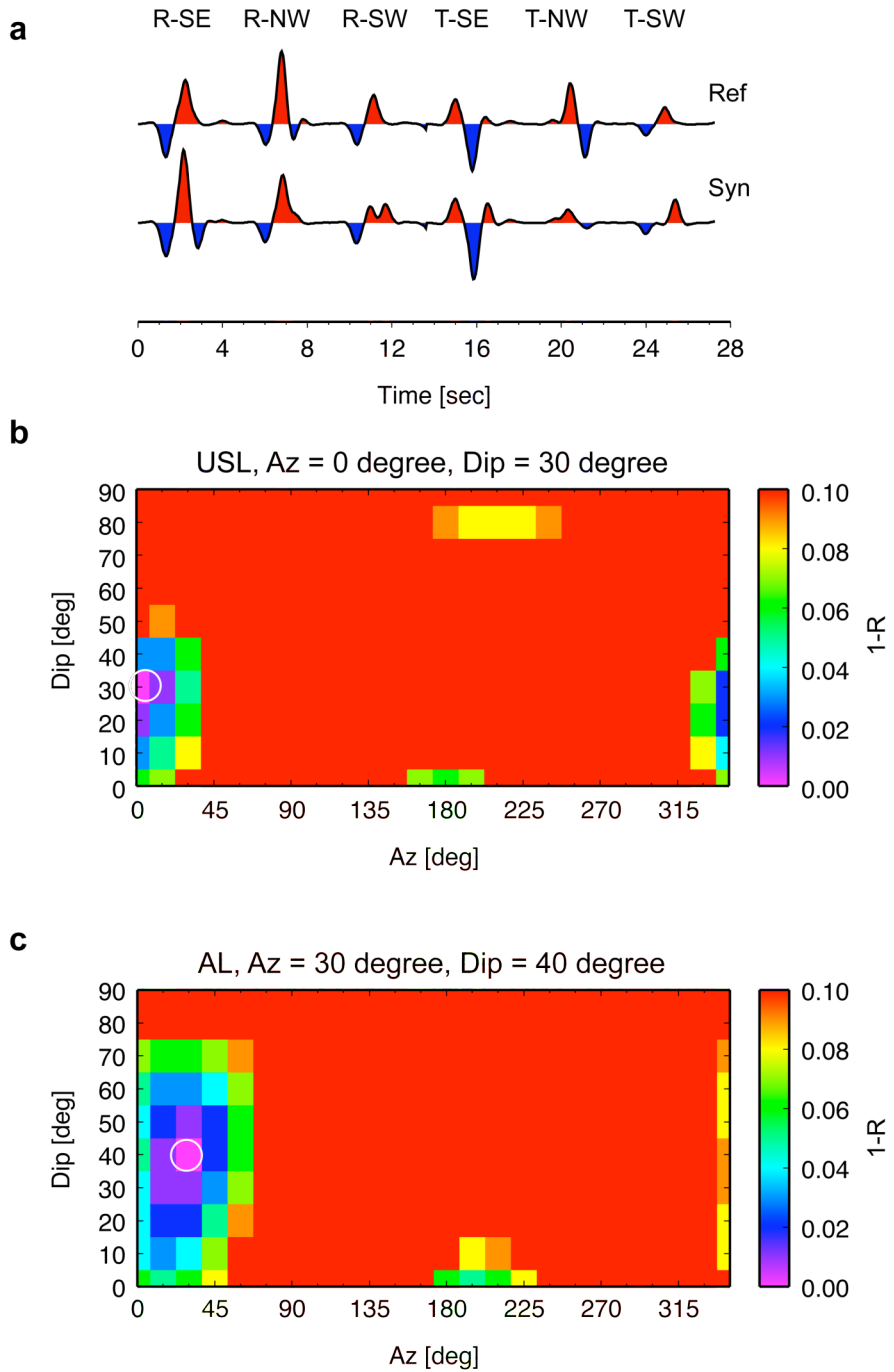
Supplementary Figure 1. Receiver function images showing the lithospheric structure from the Pacific coast to inland Mexico. (a) RRF images. (b) TRF images. The images are constructed in the frequency ranges of 0.03-1 Hz. The subducted Coco plate is initially dipping at about 18 degrees and subsequently flattened out at about 80 km inland (see also Kim et al. 2010). The amplitude of the receiver functions is scaled related to the vertical P wave.



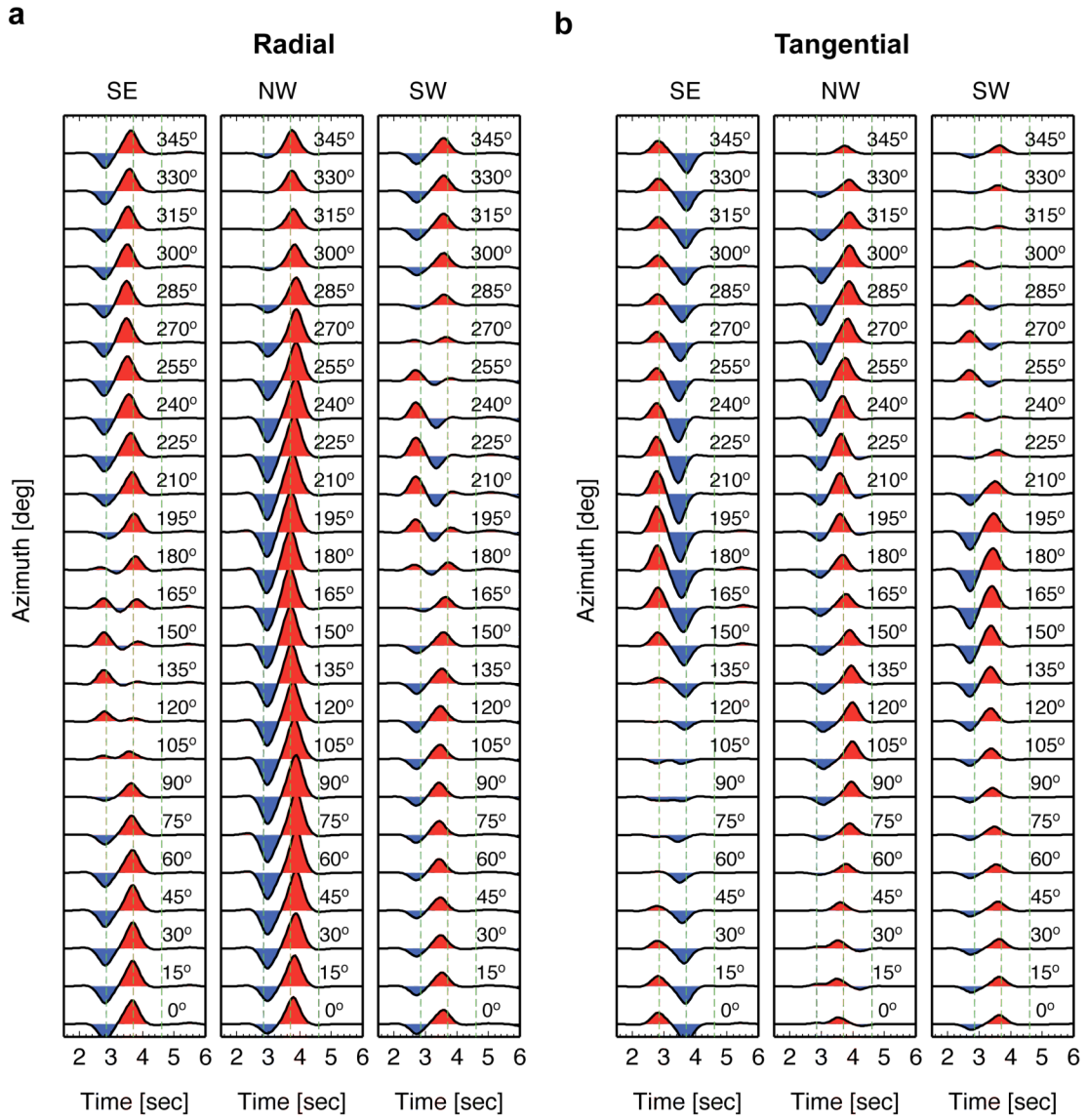
Supplementary Figure 2. Receiver function images with a different stacking scheme. Data from events within specified range of epicentral distance and back azimuth are included in constructing RRF images (A-C) and TRF images (D-F). This image displays the same feature as the image shown in Figure 3.



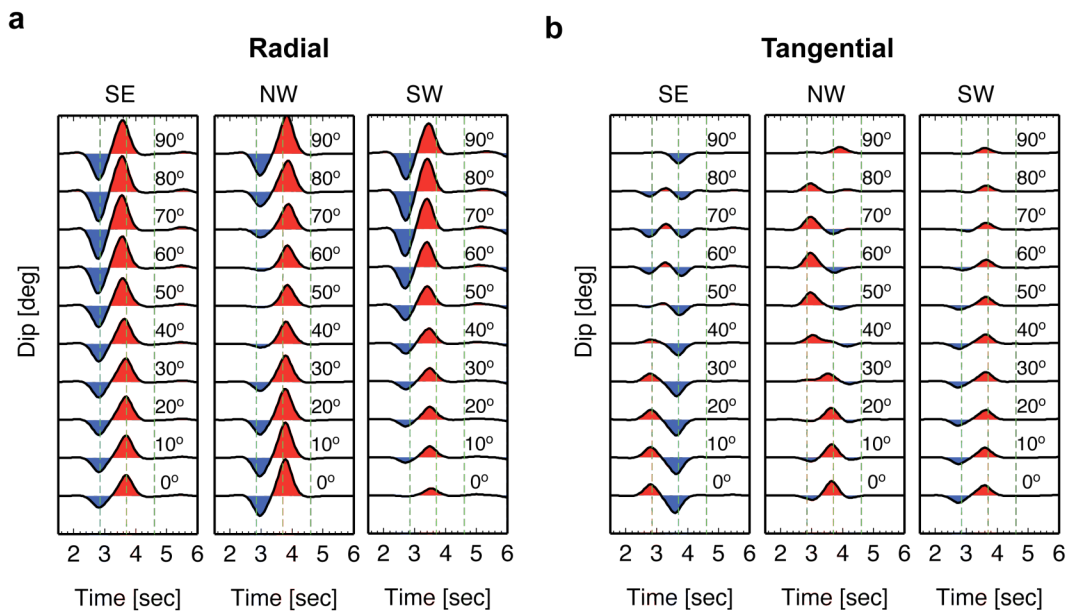
Supplementary Figure 3. Geometry of model setup in the dipping section (a) and flat section (b) of the subducted Cocos plate. The geometry of hexagonal anisotropy is shown in (c) (modified from Mercier et al. 2008). ϕ and δ are the azimuth and dipping angle of the fast symmetric axis. Note the thickness of CC is fixed at 24 km to examine the effect of slab dip. A LOC layer is added in the flat section to explain the positive energy arriving at about 4.5 seconds (see also Supplementary Fig. 12). Abbreviations are as follows: CC, continental crust; LCC, lower continental crust (tentative interpretation); USL, ultra-slow velocity layer; LOC, lower oceanic crust; AL, anisotropic layer; SOM, subducted oceanic mantle. Specific model parameters can be referred to Supplementary Table 1 and Table 2.



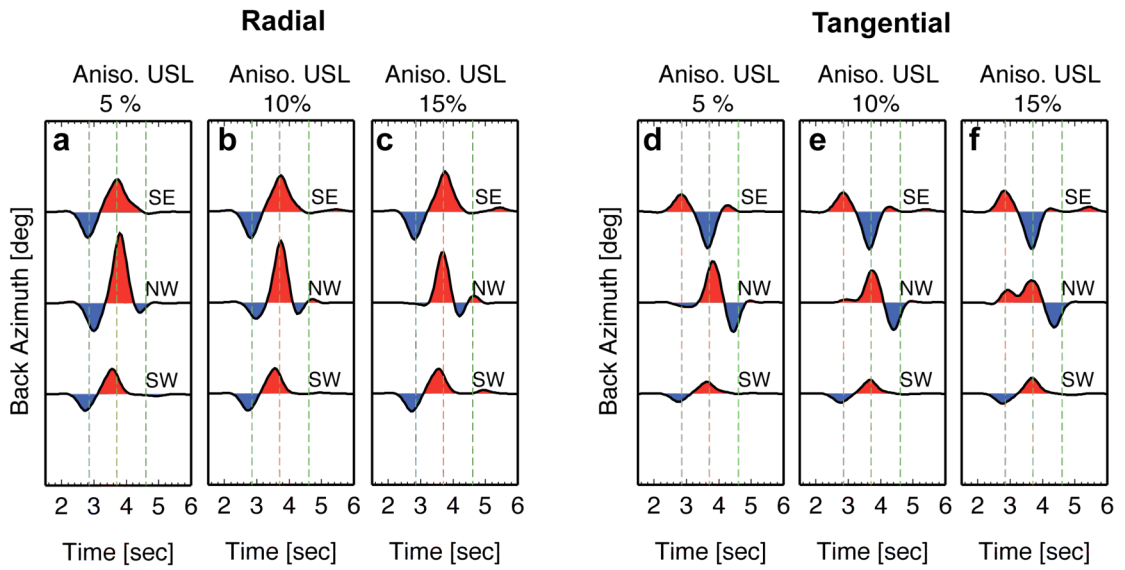
Supplementary Figure 4. Grid search result for anisotropy parameters in the USL (b) and AL (c). Synthetic RRFs and TRFs at different back azimuths SE, NW and SW are respectively concatenated before cross correlation, as illustrated in (a). R is the coefficient of cross correlation. The reference trace is computed with model parameters derived from forward trial-and-error modeling approach. The color scale indicates 1-R, a measure of the fitness. Despite the observations are limited in the SE, NW and SW, they provide a rather tight constraint on the azimuth and dip angle of the fast symmetric axis in the USL and AL, with uncertainties about ± 10 degrees. Most of the model space is covered in red, indicating low waveform similarity between the reference trace and synthetics computed with other parameters.



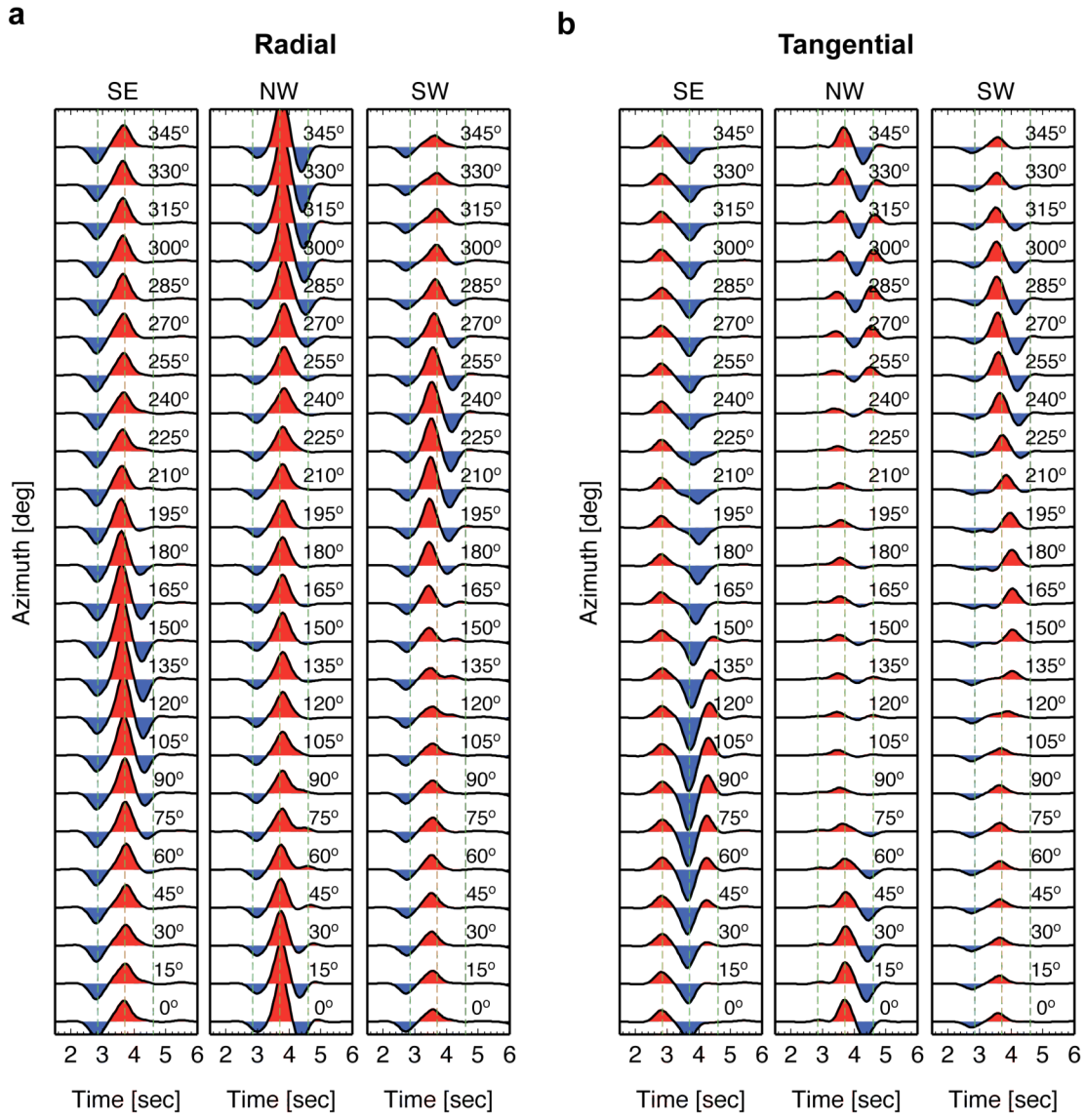
Supplementary Figure 5. Synthetic test on the azimuth of fast symmetric axis in the USL. We compute RRFs (a) and TRFs (b) at SE, NW and SW back azimuths using P-wave and S-wave anisotropy of 10%. The dip of the fast symmetric axis is fixed at 30 degrees. The preferred azimuth is at 0 degree north. We can exclude models with azimuths in the range of 45°-270° since the synthetics do not produce a stronger negative arrival in the SE swath than that in the NW swath at RRFs (a). In addition, we can also exclude models with azimuths in the range of 270°-330° since the synthetics produce a negative arrival in the NW swath at TRFs (b), which is not observed. Note the AL is not included in this test.



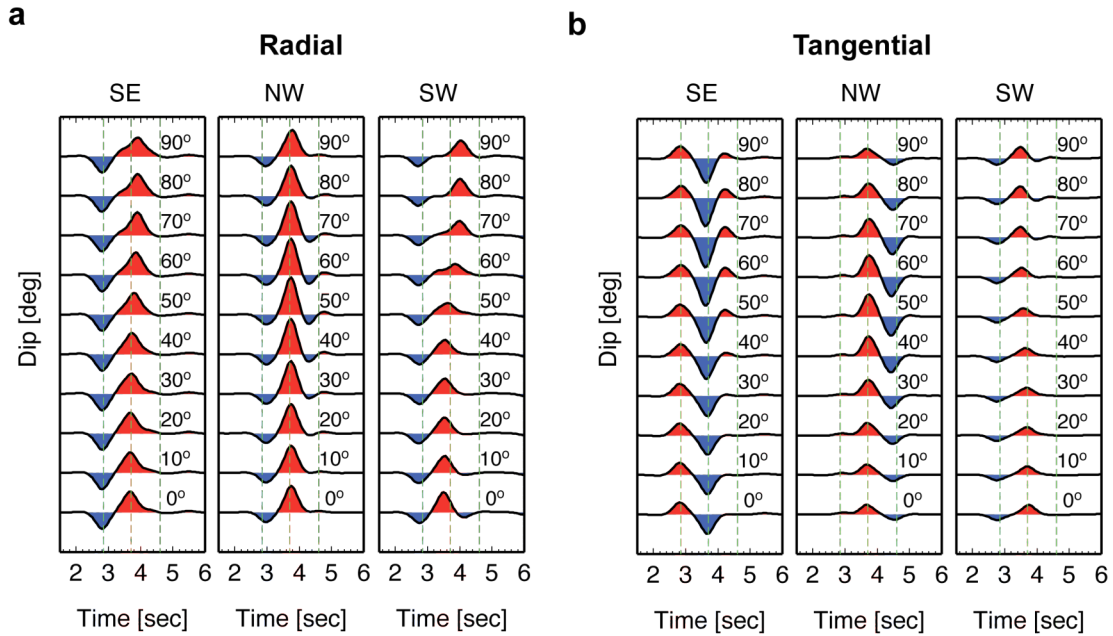
Supplementary Figure 6. Synthetic test on the dip of fast symmetric axis in the USL. We compute RRFs (a) and TRFs (b) at SE, NW and SW back azimuths using P-wave and S-wave anisotropy of 10%. The azimuth of the fast symmetric axis is fixed at 0 degree north. We can exclude models with dips in the range of 60°–90° since the synthetics predict strong signal in the SE swath RRFs (b). The preferred dip of the fast symmetric axis is 30 degrees, but weak signal in the SE swath TRFs does allow dipping angle up to 50 degrees. Note the AL is not included in this test.



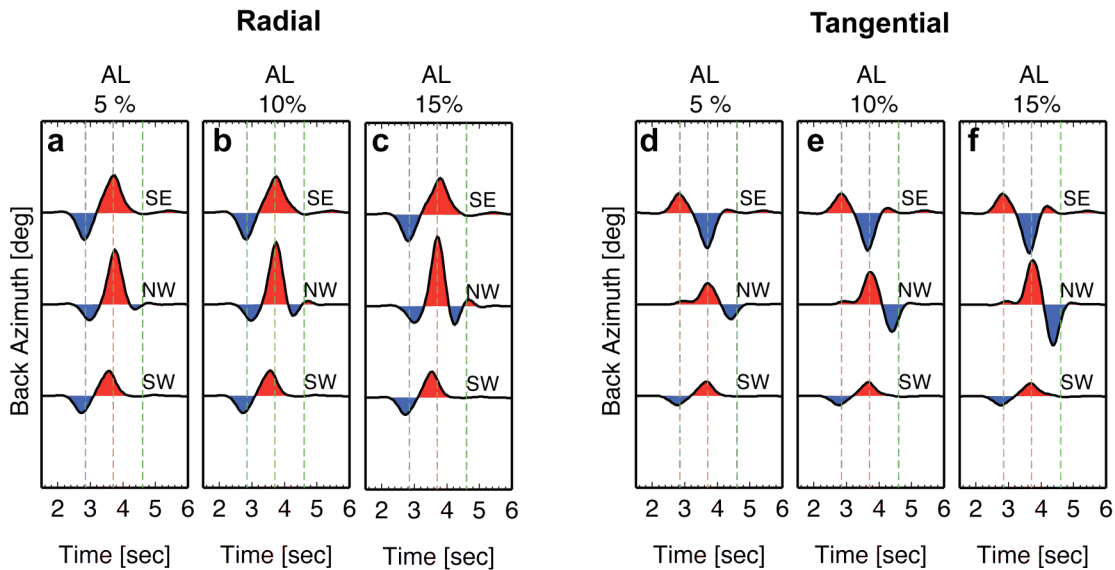
Supplementary Figure 7. Synthetic test on the strength of anisotropy in the USL. We compute RRFs (a, b, c) and TRFs (d, e, f) with P-wave and S-wave anisotropy of 5%, 10% and 15%, respectively. A 5% anisotropy in the USL do not generate a stronger negative pulse in the SE swath than that in the NW swath at RRFs (a). A 15% anisotropy in the USL appears too strong to produce observable negative pulse in the NW swath at TRFs. Note the AL is not included in this test.



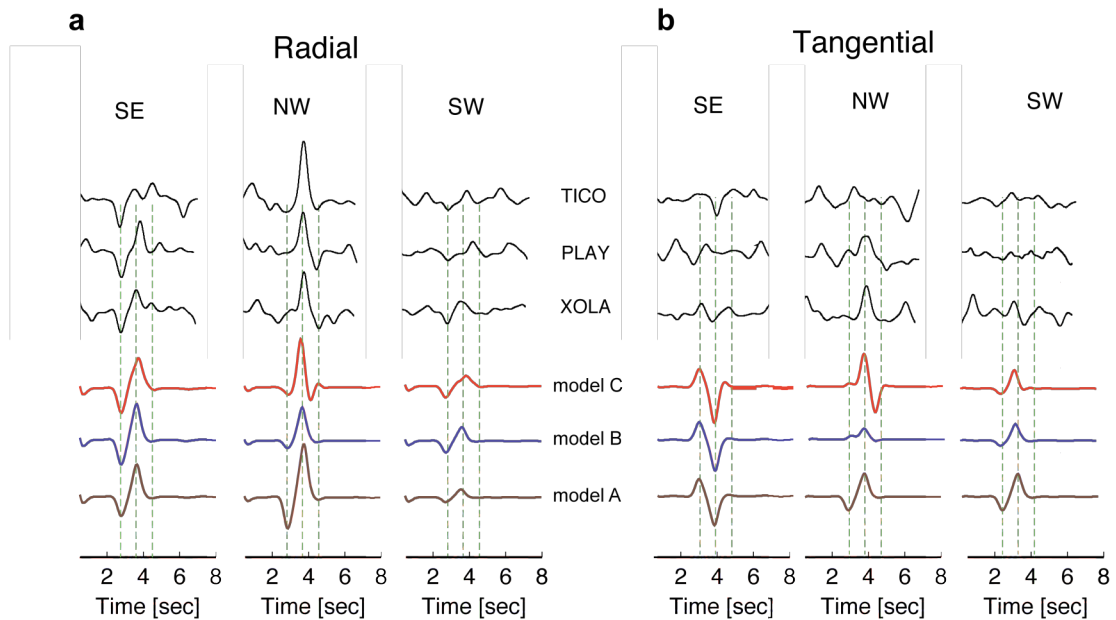
Supplementary Figure 8. Synthetic test on the azimuth of the fast symmetric axis in the AL. We compute RRFs (a) and TRFs (b) at SE, NW and SW back azimuths using P-wave and S-wave anisotropy of 10%. The dip of the fast symmetric axis is fixed at 40 degrees. We can exclude models with azimuths in the range of 60°-240° since the synthetics do not produce a stronger positive arrival in the NW swath than that in the SE swath at RRFs (a). In addition, we can also exclude models with azimuths in the range of 240°-315° since the synthetics produce a much stronger positive arrival in the SW swath than that in other back azimuths at TRFs (b), which is not observed. The preferred azimuth is at 30 degrees north. The USL is included in the synthetic test as an anisotropic layer with parameters specified in Supplementary Table 1.



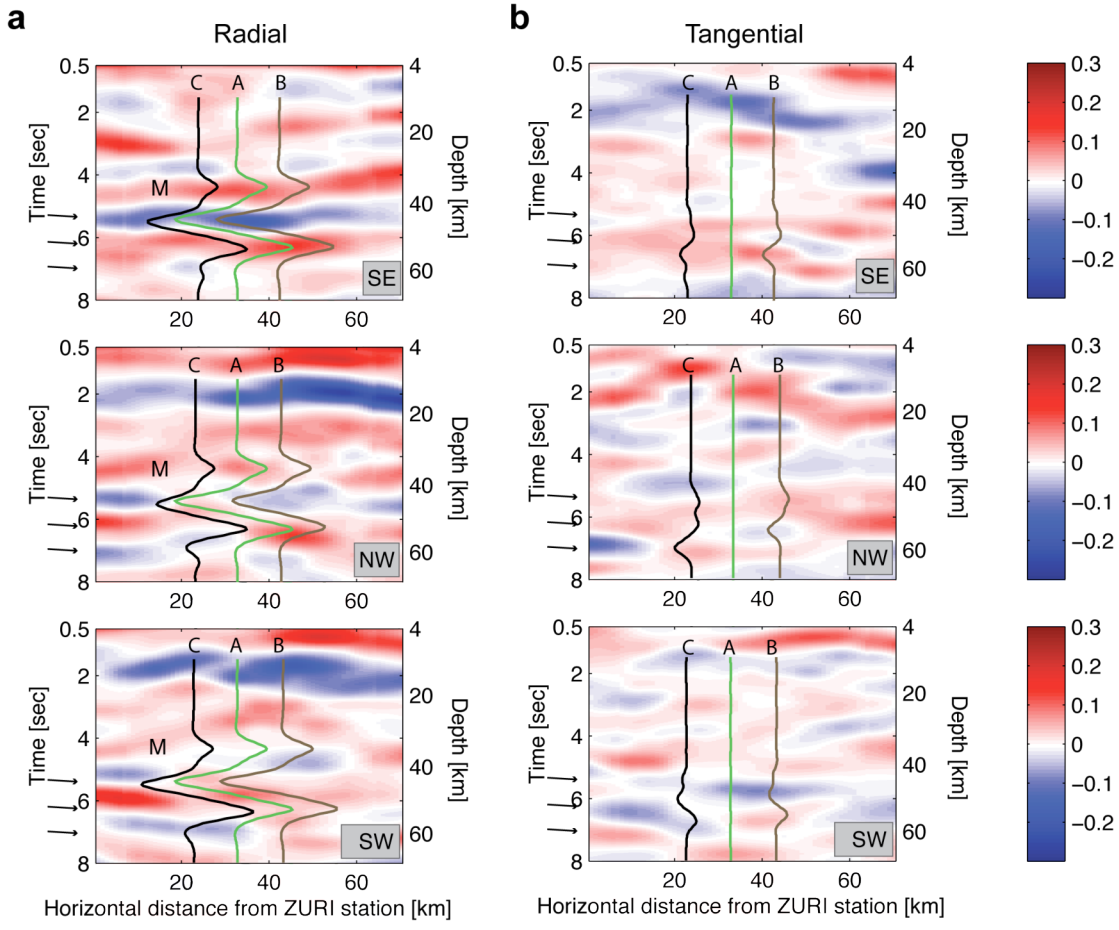
Supplementary Figure 9. Synthetic test on the dip of fast symmetric axis in the AL. We compute RRFs (a) and TRFs (b) at SE, NW and SW back azimuths using P-wave and S-wave anisotropy of 10%. The azimuth of the fast symmetric axis is fixed at 30 degrees north. We can exclude models with dips in the range of 60°-90° since the synthetics produce larger separations between positive and negative arrivals in the SW swath than observed at RRFs (a). In addition, we may also exclude models with dips in the range of 0°-20° since the synthetics produce a smaller positive arrival in the NW swath that is only 20% larger than that in the SE swath at RRFs (b), which is lower than the differences shown in the observations (~ a factor of 2). The preferred dip is about 40 degrees. The USL is included in the synthetic test as an anisotropic layer with parameters specified in Supplementary Table 1.



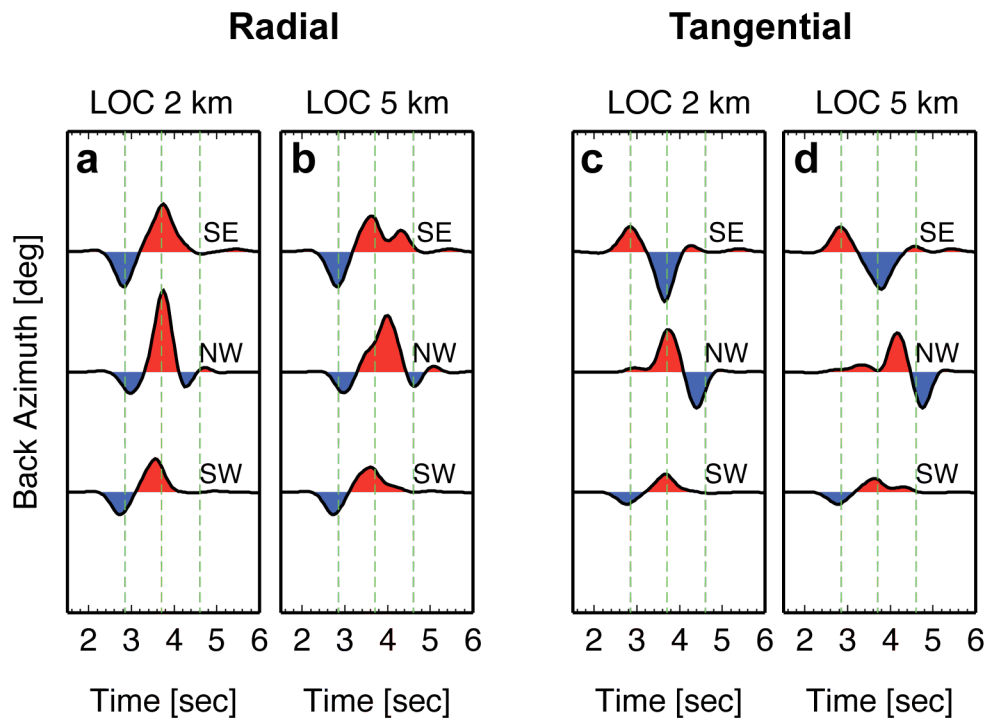
Supplementary Figure 10. Synthetic test on the strength of anisotropy in the AL. We compute RRFs (a, b, c) and TRFs (d, e, f) with P-wave and S-wave anisotropy of 5%, 10% and 15%, respectively. In general, the amplitude in TRFs is too weak for a 5% anisotropy and is too strong for a 15% anisotropy. A 15% anisotropy in the AL produces much stronger energy in the NW swath than that in the SE swath at TRFs, which is inconsistent with the observation. In addition, the TRFs appear too strong relative to the RRFs in the NW swath. The strength of S wave anisotropy is less well constrained by receiver functions alone. But we refer to velocity contrast derived from modeling local converted waves as a lower bound ($\sim 7.5\%$) to determine the strength of S-wave anisotropy at about 10%.



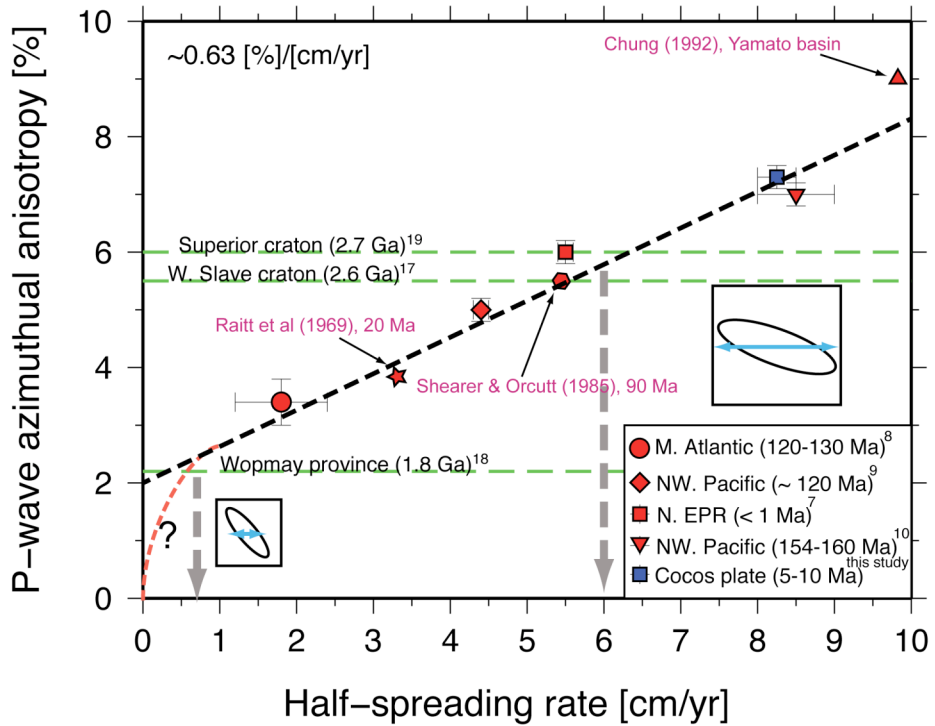
Supplementary Figure 11. Receiver function waveform comparisons for (a) RRFs and (b) TRFs. The timing of the observed receiver function has been corrected for slab dip to align with synthetics. Receiver functions in back azimuth swathes are not available due to the lack of quality events. Variabilities in the data do exist and the synthetics attempt to predict the general trend observed in each swath. The anisotropic layering is principally constrained by the local converted arrivals as well as radial receiver functions (RRFs). Tangential receive functions (TRFs) are weak and noisier while the gross feature can be better appreciated through Figure 3 and Supplementary Fig. 2. We note that weak signals observed in the SE swath TRFs can be associated with a steeper fast symmetric axis in the USL (40-50 degrees, see also Supplementary Fig. 6).



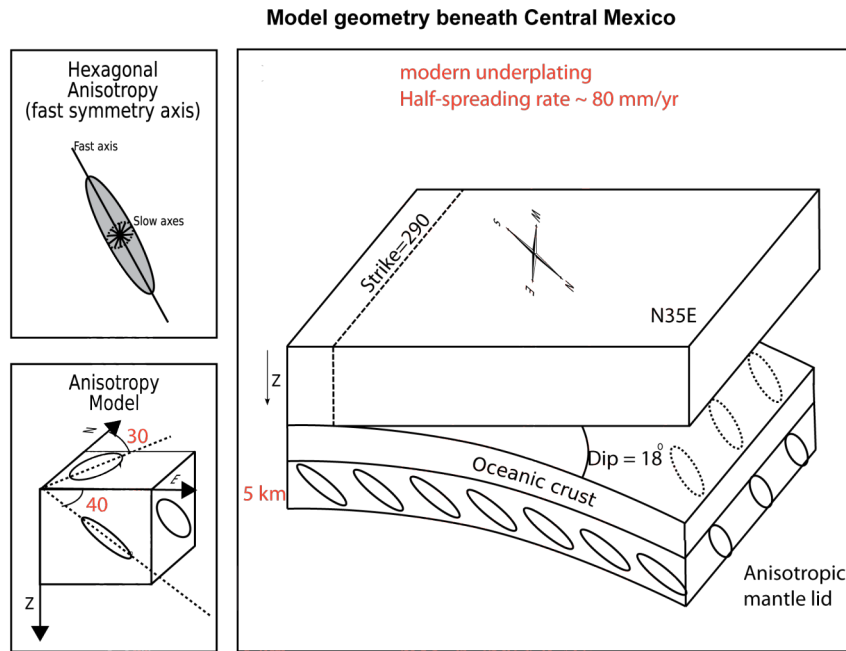
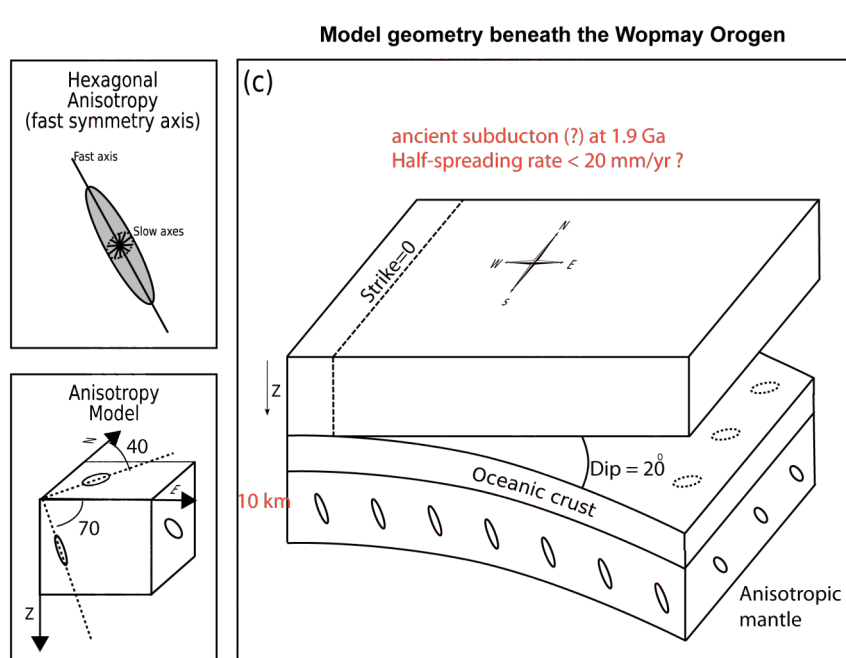
Supplementary Figure 12. Receiver function images in the flat section of subducted Cocos plate. (a) RRF images. (b) TRF images. Different from receiver function images in the dipping section of the subducted Cocos plate, the amplitude of converted waves at TRFs is relatively weak. We also display synthetics computed from our preferred anisotropic model derived from modeling receiver functions in the dipping section. The exact model parameters can be referred to Supplementary Fig. 2 and Supplementary Table 2. The dip of the fast symmetric axis in the USL and AL is therefore corrected for the slab dip, which is about 18 degree. Note the positive arrival M is possibly associated with the lower continental crust, but the signal is not continuous and less clear in the SW swath. Model A, B and C corresponds to isotropic USL, anisotropic USL, and anisotropic USL + AL, respectively. We find that receiver functions in the first 20-30 km of the flat section are better explained by the synthetics. The amplitude of predicted TRFs in the flat section is only 25 percent of that in the dipping section, which contributes to low signal-to-noise level. Variations in the amplitude of RRFs by a factor of 2 can be attributed to changes in the oceanic crust velocity (Song et al. 2009). In addition, changes in paleo spreading rate and spreading direction may also add complexities in the data.



Supplementary Figure 13. Synthetic test on the thickness of lower oceanic crust (LOC). When the thickness of the LOC increases (from 2 km to 5 km), double positive arrivals appear in the RRFs in the SE swath. Some RRFs recorded at stations such as PLAY and CARR of the MASE reveal such features (see also Fig. 5b in Kim et al. 2010), which is not inconsistent with predictions from the AL with a thick LOC. Note the positive arrival is also broadened in the RRFs in the NW swath.



Supplementary Figure 14. Same as Figure 4. We demonstrate that the linear trend established by high-quality modern seismic surveys shown in Figure 4 appears to predict a number of measurements from earlier seismic surveys by Ratt et al. (1969), Shearer & Orcutt (1985) and Chung (1992) at various oceanic plates with different ages. Note that the half-spreading rate in Yamato basin is less well determined due to relatively weak magnetic lineation, but probably faster than 10 cm/yr. Therefore, we use a lower value of 10 cm/yr in this diagram. The linear trend between P-wave azimuthal anisotropy and half-spreading rate is about 0.63 %/cm/yr after including these earlier results.

a**b**

Supplementary Figure 15. Comparisons of AML in subducted Cocos plate (a) and paleo-AML beneath the Wopmay Orogen, Canada (b) (modified from Mercier et al. 2008). The size of the ellipse is roughly proportional to the strength of anisotropy. These anisotropic mantle lids are likely representative of the mantle section of the ophiolite assemblages generated near fast and slow spreading ridges, respectively. The orientations of the fast symmetric axes in AML and paleo-AML are also consistent with mantle foliations recorded in the Oman ophiolite (inferred fast-spreading) and Trinity ophiolite (inferred slow spreading), respectively (Fig. 1 in Boudier & Nicolas, 1985).

Supplementary Table 1 Model parameters in modeling anisotropic USL and HVL in the dipping section

	TH [km]	Vp (km/s)	Vs (km/s)	Den [g/cm ³]	Vp_ani [%]	Vs_ani [%]	Dip [deg]	Az [deg]	Slab Dip	Slab strike
CC	24.0	6.6	3.7	2.7	-	-	-	-	-	-
USL	4.5	6.0	2.9	2.6	10	10	30	0	290	18.4
LOC	2.0	7.0	4.0	2.8	-	-	-	-	290	18.4
AL	4.0	8.0	4.5	3.3	10	10	40	30	290	18.4
SOM	-	8.0	4.5	3.3	-	-	-	-	290	18.4

CC: continental crust. USL: ultra-slow velocity layer. LOC: lower oceanic crust. AL: anisotropic layer. SOM: subducted oceanic mantle. $Vp_{ani} = (Vp_{fast} - Vp_{slow}) / (Vp_{fast} + Vp_{slow}) \times 200$; $Vs_{ani} = (Vs_{fast} - Vs_{slow}) / (Vs_{fast} + Vs_{slow}) \times 200$.

Supplementary Table 2 Model parameters in modeling anisotropic USL and HVL in the flat section

	TH [km]	Vp (km/s)	Vs (km/s)	Den [g/cm ³]	Vp_ani [%]	Vs_ani [%]	Dip [deg]	Az [deg]	Slab Dip	Slab strike
CC	35.0	6.6	3.7	2.7	-	-	-	-	-	-
LCC	10.0	7.5	4.1	3.1	-	-	-	-	-	-
USL	4.5	6.0	2.9	2.6	10	10	10	0	-	-
LOC	2.0	7.0	4.0	2.8	-	-	-	-	-	-
AL	4.0	8.0	4.5	3.3	10	10	20	30	-	-
SOM	-	8.0	4.5	3.3	-	-	-	-	-	-

CC: continental crust. LCC: lower continental crust. USL: ultra-slow velocity layer. LOC: lower oceanic crust. AL: anisotropic layer. SOM: subducted oceanic mantle. $Vp_{ani} = (Vp_{fast} - Vp_{slow}) / (Vp_{fast} + Vp_{slow}) \times 200$; $Vs_{ani} = (Vs_{fast} - Vs_{slow}) / (Vs_{fast} + Vs_{slow}) \times 200$.

References

1. Blackman, D. & Kendall, J.-M. Seismic anisotropy in the upper mantle, Predictions for current plate boundary flow models. *Geochem. Geophys. Geosys.* **3**, doi:10.1029/2001GC000247 (2002).
2. Bostock, M. G. Anisotropic upper-mantle stratigraphy and architecture of the Slave craton. *Nature* **390**, 392-395 (1997).
3. Bostock, M. G., Seismic imaging of lithospheric discontinuities and continental evolution. *Lithos* **48**, 1-16 (1999).
4. Boudier, F. & Nicolas, A. Harzburgite and Iherzolite subtypes in ophiolite and oceanic environments. *Earth Planet. Sci. Lett.* **76**, 84-92 (1985).
5. Christensen, N. I. & Salisbury, M. H. Seismic anisotropy in the oceanic upper mantle: Evidence from the Bay of Islands Ophiolites Complex. *J. Geophys. Res.* **84**, 4601-4610 (1979).
6. Christensen, N. I. The magnitude, symmetry and origin of upper mantle anisotropy based on fabric analyses of ultramafic tectonites. *Geophys. J. R. Astr. Soc.* **76**, 89-111 (1984).
7. Ceuleneer, G., Nicolas, A. & Boudier, F. Mantle flow patterns at an oceanic spreading center: The Oman peridotites record. *Tectonophysics* **151**, 1-26 (1988).
8. Chung, T. W. An quantitative of seismic anisotropy in the Yamato Basin, the southeast Japan Sea, from refraction data from an ocean bottom seismic array. *Geophys. J. Int.* **109**, 620-638 (1992).
9. Currie, C. A., Hyndman, R. D., Wang, K. Thermal models of the Mexico subduction zone: Implications for the megathrust seismogenic zone. *J. Geophys. Res.* **107**, doi: 10.1029/2001JB000886 (2002).

10. Faccenda, M., Gerya, T. & Chakraborty, S. Styles of post-subduction collisional orogeny: Influence of convergence velocity, crustal rheology and radiogenic heat production. *Lithos*. **103**, 257-287 (2008).
11. Forsyth, D. W., Webb, S. C., Dorman, L. M. & Shen, Y. Phase velocities of Rayleigh waves in the MELT experiment on the East Pacific Rise. *Science* **280**, 1235-1238 (1998).
12. Hacker, B. R., Abers, G. A. & Peacock, S. M. Subduction factory 1. Theoretical mineralogy, densities, seismic wave speeds, and H₂O contents. *J. Geophys. Res.* **108**, doi: 10.1029/2001JB001127 (2003).
13. Herzberg, C., Condie, K. & Korenaga, J. Thermal history of the Earth and its petrological expression. *Earth Planet. Sci. Lett.* **292**, 79-88 (2010).
14. Hoffman, P. F. & Bowring, S. A. Short-lived 1.9 Ga continental margin and its destruction, Wopmay orogen, northwest Canada. *Geology* **12**, 68-72 (1984).
15. Ismail, W. B. & Mainprice, D. An olivine fabric database: an overview of upper mantle fabrics and seismic anisotropy. *Tectonophysics* **296**, 145-197 (1998).
16. Karato, S. & Jung, H. Water, partial melting and the origin of the seismic low velocity and high attenuation zone in the upper mantle. *Earth Planet. Sci. Lett.* **157**, 193-207 (1998).
17. Kim, Y., Clayton, R. W. & Jackson, J. M. Geometry and seismic properties of the subducting Cocos plate in central Mexico. *J. Geophys. Res.* **115**, doi:10.1029/2009JB006942 (2010).
18. Korenaga, J. Archean geodynamics and the thermal evolution of Earth. *Archean Geodynamics and Environments, AGU Monograph Series* **164**, 7-32 (2006).

19. Masacchio, G., White, D. J., Asudeh, I. & Thomson, C. J. Lithospheric structure and composition of the Archaean western Superior Province from seismic refraction/wide-angle reflection and gravity modelling. *J. Geophys. Res.* **109**, doi:10.1029/2003JB002427 (2004).
20. Mercier, J.-P. et al. The teleseismic signature of fossil subduction: Northwestern Canada. *J. Geophys. Res.* **113**, doi: 10.1029/2007JB005127 (2008).
21. Nicolas, A. & Violette, J. F. Mantle flow at oceanic spreading centers: models derived from ophiolites. *Tectonophysics* **81**, 319-339 (1982).
22. O'Neill, C., Lenardic, A., Moresei, L., Torsvik, T. H. & Lee, C-T. A. Episodic Precambrian subduction. *Earth Planet. Sci. Lett.* **262**, 552-562 (2007).
23. Raitt, R. W., Shor, G. G., Francies, T. J. G. & Morris, G. B. Anisotropy of the Pacific upper mantle. *J. Geophys. Res.* **74**, 3095-3109 (1969).
24. Shearer, P. & Orcutt, J. Anisotropy in the lithosphere – theory and observations from the Ngendei seismic refraction experiment in the south-west Pacific. *Geophys. J. R. Astr. Soc.* **80**, 493-526 (1985).
25. Silver, P. G. & Behn, M. Intermittent plate tectonics. *Science* **319**, 85-88 (2008).
26. Sizova, E., Gerya, T., Brown, M. & Perchuk, L. L. Subduction styles in the Precambrian: Insight from numerical experiments. *Lithos.* **116**, 209-229 (2010).
27. Song, T.-R. A. et al. Subducting slab ultra-slow velocity layer coincident with silent earthquake in southern Mexico. *Science*. **324**, 502-506 (2009).

28. Zhang, S. & Karato, S. Lattice preferred orientation of olivine aggregates deformed in simple shear. *Nature* **375**, 774-777 (1995).